

Magnetic phase diagrams of barcode-type nanostructures

This article has been downloaded from IOPscience. Please scroll down to see the full text article.

2009 Nanotechnology 20 385703

(<http://iopscience.iop.org/0957-4484/20/38/385703>)

[The Table of Contents](#) and [more related content](#) is available

Download details:

IP Address: 158.170.250.246

The article was downloaded on 28/08/2009 at 17:21

Please note that [terms and conditions apply](#).

Magnetic phase diagrams of barcode-type nanostructures

B Leighton^{1,2}, O J Suarez³, P Landeros³ and J Escrig^{1,2}

¹ Departamento de Física, Universidad de Santiago de Chile (USACH), Avenida Ecuador 3493, 917-0124 Santiago, Chile

² Centro para el Desarrollo de la Nanociencia y Nanotecnología, CEDENNA, 917-0124 Santiago, Chile

³ Departamento de Física, Universidad Técnica Federico Santa María, Avenida España 1680, Casilla 110 V, 2340000 Valparaíso, Chile

E-mail: juan.escrig@usach.cl

Received 14 April 2009, in final form 6 July 2009

Published 28 August 2009

Online at stacks.iop.org/Nano/20/385703

Abstract

The magnetic configurations of barcode-type magnetic nanostructures consisting of alternate ferromagnetic and nonmagnetic layers arranged within a multilayer nanotube structure are investigated as a function of their geometry. Based on a continuum approach we have obtained analytical expressions for the energy which lead us to obtain phase diagrams giving the relative stability of characteristic internal magnetic configurations of the barcode-type nanostructures.

(Some figures in this article are in colour only in the electronic version)

1. Introduction

Magnetic nanoparticles are attracting the increasing interest of researchers in various fields due to their promising applications in hard disk drives, magnetic random access memory, and other spintronic devices [1–5]. In addition, these magnetic nanoparticles can be used for potential biomedical applications, such as magnetic resonance imaging (the nanoparticles can be used to trace bioanalytes in the body), cell and DNA separation, and drug delivery [6]. To apply nanoparticles in various potential devices and architectures, it is very important to control their size and shape in order to retain thermal and chemical stability [7].

The trusty sphere remains the preferred shape for nanoparticles, but this geometry leaves only one surface for modification, complicating the generation of multifunctional particles. Thus, a technology that could modify differentially the inner and outer surfaces would be highly desirable [8]. Tubular nanostructures have stimulated extensive research efforts in recent years because of their particular significance for prospective applications. A wide range of materials including semiconductors, polymers, and metals have been prepared in the form of nanotubes [9–13]. Although magnetic nanotubes has been intensively investigated, barcode-type nanostructures have received less attention, in spite of tailoring their multisegmented nanotube structure, along with the

functionalization of the inner wall surface of barcode-type nanotubes with various molecules (for example, proteins and DNA). Moreover, they are expected to be particularly useful in the field of catalysis, advanced microfluidics, molecule separation, and biological and magnetic sensors [14–19]. It is worth mentioning that barcode-type magnetic nanostructures consisting of regular arrays of magnetic segments have been considered as providing the basis for extending magnetic storage densities beyond the superparamagnetic limit. In such a system, a single tube with n magnetic layers might store up to 2^n bits, with a volume much larger than those of the grains in conventional recording media, beating this way thermal fluctuations and increasing the recording density by a factor 2^{n-1} [20, 21]. Recently [14], the preparation of metallic nanotubes based on the preferential electrodeposition of metal along the pore walls of an anodic alumina oxide (AAO) membrane, in the presence of metallic nanoparticles on the wall surfaces, has been reported. In the paper by Lee *et al* [14] multisegmented metallic nanotubes were prepared, with a bimetallic stacking configuration along the tube axis, showing different magnetic behavior as compared with continuous ones, which encourages a study of the possible magnetic configurations and magnetostatic interactions in these barcode-type magnetic nanotubes. Clearly, for the development of magnetic devices based on those arrays, knowledge of the internal magnetic structure of the barcode-type nanostructures is of fundamental importance.

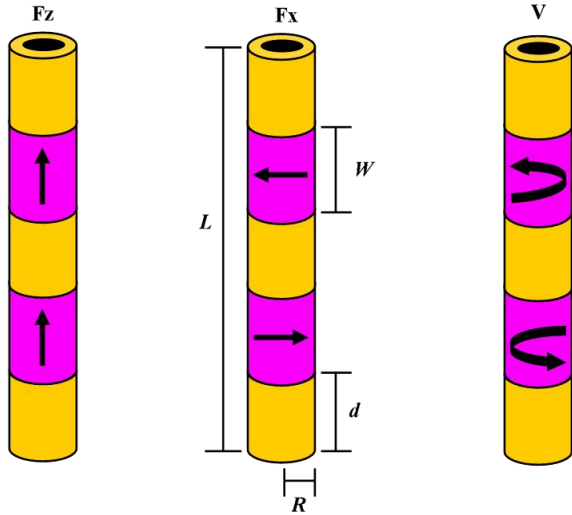


Figure 1. Geometrical parameters and magnetic configurations of barcode-type nanostructures.

The purpose of this paper is to investigate the magnetic ordering of barcode-type nanostructures. Our particles are characterized by a set of geometrical parameters, as depicted in figure 1. The first are their external and internal radii, R and a , respectively, and the total length, L , which includes the magnetic matter as well as the nonmagnetic matter. It is convenient to define the ratio $\beta \equiv a/R$, so that $\beta = 0$ represents a solid cylinder and $\beta \rightarrow 1$ corresponds to a very narrow tube. We denote by W the length of each ferromagnetic segment and by d the length of each nonmagnetic portion, so that, if we have a barcode-type structure with n magnetic tubes, the total length can be written as $L = nW + (n + 1)d$.

2. Model and discussion

We adopt a simplified description of the magnetic system in which the discrete distribution of magnetic moments is replaced by a continuous one, defined by the magnetization vector field $\mathbf{M}(\mathbf{r})$ such that $\mathbf{M}(\mathbf{r})\delta v$ gives the total magnetic moment within an elementary volume δv centered at \mathbf{r} . The total magnetic energy (E_{tot}) is generally given by the sum of four terms: exchange, dipolar, anisotropy and Zeeman contributions, which are taken from the well known continuum theory of ferromagnetism [22]. As we are interested in the study of the relative stability of the zero-field magnetic ground states, the contribution of the Zeeman energy can be ignored. Under these assumptions, the magnetic energy is just given by the dipolar (E_{dip}), exchange (E_{ex}), and anisotropy (E_k) contributions.

The total magnetization can be written as $\mathbf{M}(\mathbf{r}) = \sum_{i=1}^n \mathbf{M}_i(\mathbf{r})$, where $\mathbf{M}_i(\mathbf{r})$ is the magnetization of the i th ferromagnetic segment. In this case, the magnetostatic potential $U(\mathbf{r})$ splits up into n components, $U_i(\mathbf{r})$, associated with the magnetization of each ferromagnetic segment. Then, the total dipolar energy can be written as $E_{\text{dip}} =$

$\sum_{i=1}^n E_{\text{dip}}(i) + \sum_{i=1}^{n-1} \sum_{j=i+1}^n E_{\text{int}}(i, j)$, where

$$E_{\text{dip}}(i) = \frac{\mu_0}{2} \int \mathbf{M}_i(\mathbf{r}) \cdot \nabla U_i(\mathbf{r}) dv$$

is the dipolar contribution to the self-energy of the i th ferromagnetic segment, and

$$E_{\text{int}}(i, j) = \mu_0 \int \mathbf{M}_i(\mathbf{r}) \cdot \nabla U_j(\mathbf{r}) dv$$

is the dipolar interaction between ferromagnetic segments i and j .

Usually, the exchange energy E_{ex} in multilayer nanostructures has contributions both from the direct exchange interaction within the magnetic segments and from the indirect interaction between them, mediated by the conduction electrons in the nonmagnetic layers. Since the indirect interaction decays rapidly with the thickness of the nonmagnetic segment, it can be neglected provided d is large enough. A good estimate of the range of the indirect exchange interaction can be obtained from the results for multilayers [23]. As a general result, the interlayer exchange coupling vanishes for spacer thicknesses greater than a few nanometers, which does not exceed the value of the exchange length $l_x = \sqrt{2A/\mu_0 M_0^2}$ of ferromagnetic metals. Here we focus our attention on those cases in which d is not smaller than the magnetic material's l_x , such as the tubes fabricated by Lee *et al* [14] which satisfy $d \gg l_x$, and thus the interlayer exchange coupling can be safely neglected. Therefore, to a good approximation, we can write $E_{\text{ex}} = \sum_{i=1}^n E_{\text{ex}}(i)$, where $E_{\text{ex}}(i) = A \int [(\nabla m_{ix})^2 + (\nabla m_{iy})^2 + (\nabla m_{iz})^2] dv$. Here, $\mathbf{m}_i = (m_{ix}, m_{iy}, m_{iz}) = \mathbf{M}_i/M_0$ is the magnetization, normalized to the saturation magnetization M_0 , and A is the stiffness constant of the magnetic material.

The cubic anisotropy energy of the particle can be added by means of the following expression:

$$E_c(i) = K_c \int (m_{ix}^2 m_{iy}^2 + m_{iy}^2 m_{iz}^2 + m_{iz}^2 m_{ix}^2) dv,$$

and the uniaxial anisotropy energy is given by

$$E_u(i) = -K_u \int m_{iz}^2 dv.$$

On the basis of the above results, the total energy of the barcode-type nanostructure can be written as $E_{\text{tot}} = \sum_{i=1}^n E_{\text{self}}(i) + \sum_{i=1}^{n-1} \sum_{j=i+1}^n E_{\text{int}}(i, j)$, where $E_{\text{self}}(i) = E_{\text{dip}}(i) + E_{\text{ex}}(i) + E_k(i)$ is the self-energy of the ferromagnetic segment i , and E_{int} is the (dipolar) interaction energy between two magnetic segments. We will proceed to describe the magnetization of the different states we are considering here and then we will evaluate the magnetic energy of each configuration. Results will be given in units of $\mu_0 M_0^2 l_x^3$, i.e., $\tilde{E} = E/\mu_0 M_0^2 l_x^3$.

2.1. Magnetic configurations

It has been shown recently that single magnetic nanorings present three basic ground states depending on their geometry

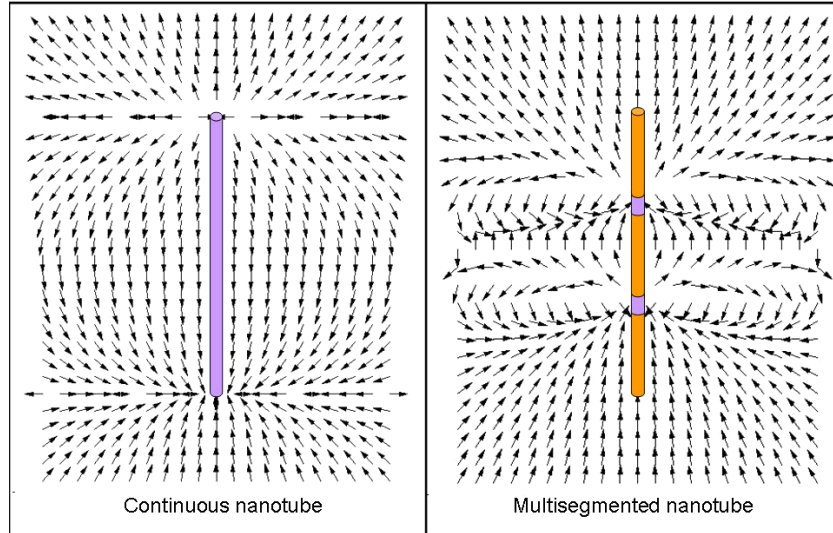


Figure 2. Stray field direction (arrows) generated by a single nanotube (*left picture*) and a multisegmented nanotube (*right picture*) magnetized in the $+z$ direction. These two examples correspond to nanotubes with the same geometrical parameters as those studied experimentally by Lee *et al* [14].

(see figure 1) [24, 25]. These configurations are: (Fz) a quasi-uniform magnetization state oriented in the direction parallel to the cylindrical axis (z axis); (Fx) a quasi-uniform magnetization state oriented in the plane perpendicular to the z axis; and (V) a flux-closure vortex state. For long nanorings ($W \gg R$), the Fx phase is not present [24, 25], a result that holds for nanotubes [26, 27].

It has been shown by Rothman *et al* [28] that for magnetized nanorings the single-domain in-plane ground state is the *onion* state. In addition, the single-domain axial state for rings with a small inner diameter might be similar to the *flower* state expected in thick axially magnetized cylinders [29]. Therefore, it may appear questionable to select the uniform in-plane and axial states as single-domain states to build the phase diagram upon, as they are not stable configurations at a zero applied field. However, it has been verified by micromagnetic simulations [24] and analytical calculations [25] that the energy difference between the actual single-domain ground state in a nanoring, and the uniform state, often turns out to be very small. From this available evidence, we conclude that the replacement of the more correct quasi-uniform states by simpler ideal uniform states, only results in uncertainties in the exact location of the phase boundaries and some of the physical values extracted from the phase diagram.

2.1.1. Fz state. For the Fz state, where the magnetization of the n ferromagnetic segments is uniform and parallel to the z axis, $\mathbf{M}(\mathbf{r})$ can be approximated by $M_0\hat{z}$, where \hat{z} is the unit vector parallel to the axis of the nanotube. In this case the exchange contribution to the self-energy vanishes, and the reduced self-energy takes the form [26]

$$\tilde{E}_{\text{self}}^{Fz} = \frac{\pi R^3}{l_x^3} \int_0^\infty \frac{dq}{q^2} (1 - e^{-q\frac{W}{R}}) (J_1(q) - \beta J_1(q\beta))^2 - \frac{\kappa_u \pi W R^2}{2 l_x^3} (1 - \beta^2),$$

where $J_1(z)$ is a Bessel function of the first kind and $\kappa_u = 2K_u/\mu_0 M_0^2$. In order to calculate the interaction energy between the ferromagnetic segments, we first need to calculate the magnetostatic potential $U(\mathbf{r})$ of a single tubular structure. The expression for this potential has been previously reported [30] and is given by

$$U(r, z) = \frac{M_0}{2} \int_0^\infty \frac{dk}{k} J_0(kr) [R J_1(kR) - a J_1(ka)] \times (e^{-k|\frac{W}{2}-z|} - e^{-k|\frac{W}{2}+z|}).$$

From this equation it is possible to obtain the expression for the magnetostatic field. Thus we write, $\mathbf{H}(r, z) = -\nabla U(r, z) = H_r(r, z)\hat{r} + H_z(r, z)\hat{z}$ with

$$H_r(r, z) = \frac{M_0}{2} \int_0^\infty dk J_1(kr) [R J_1(kR) - a J_1(ka)] \times (-e^{-k|\frac{W}{2}-z|} + e^{-k|\frac{W}{2}+z|})$$

and

$$H_z(r, z) = \frac{M_0}{2} \int_0^\infty dk J_0(kr) \times [R J_1(kR) - a J_1(ka)] Y(W, z),$$

where

$$Y(W, z) = \text{sign}\left(\frac{W}{2} - z\right) e^{-k|\frac{W}{2}-z|} - \text{sign}\left(-\frac{W}{2} - z\right) e^{-k|-\frac{W}{2}-z|}.$$

The function $\text{sign}(x)$ gives -1 , 0 or 1 depending on whether x is negative, zero, or positive. Figure 2 illustrates the magnetostatic field profile calculated analytically for nanotubes with the same geometrical parameters as the ones investigated experimentally by Lee *et al* [14]. Finally, the reduced interaction energy between two tubular nanostructures

has been calculated in a rather general way by Escrig *et al* [21, 30] and is given by

$$\tilde{E}_{\text{int}}^{Fz}[d] = -\frac{\pi R^3}{l_x^3} \int_0^\infty \frac{dq}{q^2} e^{-q\frac{d}{R}} (1 - e^{-q\frac{W}{R}})^2 \times (J_1(q) - \beta J_1(q\beta))^2.$$

Thus, the reduced total energy for the Fz state can be expressed as

$$\tilde{E}_{\text{tot}}^{Fz} = n\tilde{E}_{\text{self}}^{Fz} - \frac{\pi R^3}{l_x^3} \int_0^\infty \frac{dq}{q^2} e^{-q\frac{W}{R}} (1 - e^{-q\frac{W}{R}}) \times (J_1(q) - \beta J_1(q\beta))^2 g_z(n, q, \sigma),$$

where

$$g_z(n, q, \sigma) = \frac{(n-1)e^{q\sigma} + e^{-(n-1)q\sigma} - n}{(1 - e^{q\sigma})^2} \quad \text{and} \quad \sigma = \frac{d+W}{R}.$$

2.1.2. Fx state. For the Fx state, $\mathbf{M}(\mathbf{r})$ can be generally considered as $M_0 \cos[(i-1)\theta]\hat{x} + M_0 \sin[(i-1)\theta]\hat{y}$, which represent a helicoidal magnetic state, with θ the angle between the in-plane magnetization of adjacent segments. For the in-plane state, the exchange and anisotropy contributions to the self-energy vanish and the reduced self-energy takes the form [21]

$$\tilde{E}_{\text{self}}^{Fx} = \frac{\pi R^3}{2l_x^3} \int_0^\infty \frac{dq}{q^2} \left(e^{-q\frac{W}{R}} + q\frac{W}{R} - 1 \right) \times (J_1(q) - \beta J_1(q\beta))^2,$$

where $J_1(z)$ is a Bessel function of the first kind. In order to calculate the interaction energy between the ferromagnetic segments, we first need to calculate the magnetostatic potential $U(\mathbf{r})$ of a single tubular structure. The expression for this potential is given by

$$U(r, \phi, z) = M_0 \cos \phi \int_0^\infty \frac{dk}{k} J_1(kr) f(k) \times \begin{cases} e^{-kz} \sinh\left(k\frac{W}{2}\right) & z > \frac{W}{2} \\ (1 - e^{-k\frac{W}{2}}) \cosh(kz) & -\frac{W}{2} < z < \frac{W}{2} \\ e^{kz} \sinh\left(k\frac{W}{2}\right) & z < -\frac{W}{2}, \end{cases}$$

where $f(k) = (RJ_1(kR) - aJ_1(ka))$. Finally, the reduced interaction energy between two tubular nanostructures is given by

$$\tilde{E}_{\text{int}}^{Fx}[d, \theta] = \frac{\pi R^3}{2l_x^3} \cos \theta \int_0^\infty \frac{dq}{q^2} e^{-q\frac{d}{R}} (1 - e^{-q\frac{W}{R}})^2 \times (J_1(q) - \beta J_1(q\beta))^2.$$

Thus, the reduced total energy for the Fx state can be expressed as

$$\tilde{E}_{\text{tot}}^{Fx} = n\tilde{E}_{\text{self}}^{Fx} + \frac{\pi R^3}{2l_x^3} \int_0^\infty \frac{dq}{q^2} e^{-q\frac{W}{R}} (1 - e^{-q\frac{W}{R}})^2 \times (J_1(q) - \beta J_1(q\beta))^2 g_x(n, q, \sigma, \theta),$$

Table 1. Parameters for different materials taken from [31]. Uniaxial (K_u) cobalt is denoted with a superscript.

Material	K (J m ⁻³)	κ
Iron	4.8×10^4	0.0264
Cobalt ^a	4.1×10^5	0.3329
Permalloy	-3.0×10^2	-0.0007
Nickel	-4.5×10^3	-0.0304

^a Iron, permalloy and nickel have cubic (K_c) anisotropy.

where

$$g_x(n, q, \sigma, \theta) = \sum_{i=1}^{n-1} \sum_{j=i+1}^n e^{-q\sigma(j-i)} \cos[(j-i)\theta]$$

and

$$\sigma = \frac{d+W}{R}.$$

From this expression we can conclude that for zero applied field the total energy of this state is further reduced for the value $\theta = \pi$, independently of the value of n . Thus, for the particular case when $\theta = \pi$ we obtain

$$g_x(n, q, \sigma, \pi) = -\frac{e^{q\sigma(1-n)}[(-1)^n - e^{nq\sigma}] + (1 + e^{q\sigma})n}{(1 + e^{q\sigma})^2}.$$

2.1.3. Vortex state. Finally, for the vortex state V , $\mathbf{M}(\mathbf{r})$ can be approximated by $M_0\hat{\phi}$, where $\hat{\phi}$ is the azimuthal unit vector. Due to the condition of perfect flux closure in the vortex configuration, one magnetic nanostructure in such a configuration does not interact with the others, independently of their magnetic configuration. Thus, there is no difference between the clockwise and counter-clockwise directions. Finally, the reduced total energy for the vortex state is given just by the n self-energies [21, 26]

$$\tilde{E}^V = -n\frac{\pi W \ln \beta}{l_x} + n\frac{\kappa_c}{16} \frac{\pi W R^2}{l_x^3} (1 - \beta^2).$$

Here, $\kappa_c = 2K_c/\mu_0 M_0^2$.

2.2. Phase diagram for multisegmented nanorings

We proceed to investigate the relative stability of the configurations. Phase diagrams are shown in figure 3 for $d = l_x$, $\beta = 0.5$, and $n = 5$. The anisotropy for four different materials are considered according to the values presented in table 1. The diagrams show three regions, corresponding to configurations Fz , Fx , and V , as in the case of a single nanoring ($n = 1$). Notice that for the case of Co, the existence of a strong uniaxial anisotropy favors the Fz phase, decreasing the other two phases, specially the V one. In the case of cubic anisotropy, the transition lines are similar to the case of a phase diagram without anisotropy. Because of its very low anisotropy, results for permalloy describe reasonably well a material with no anisotropy, as was pointed out in [27].

Since nanostructures are usually polycrystalline, the crystallographic orientations of the crystallites are random and,

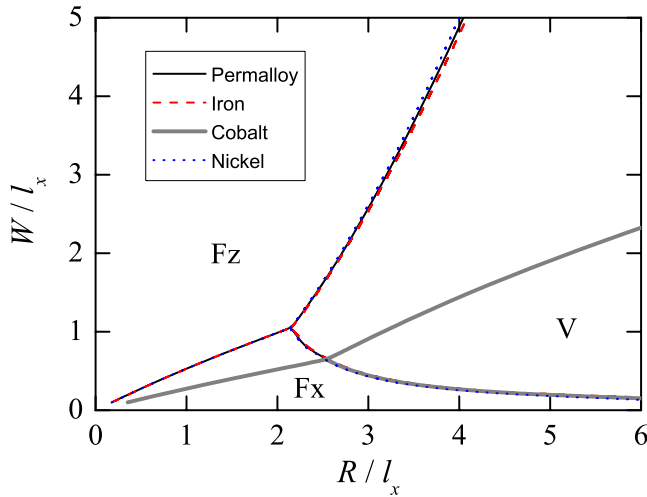


Figure 3. Phase diagrams for barcode-type nanostructures giving the regions in the RW plane where one of the configurations has lower energy. We have used $\beta = 0.5$, $d = l_x$, and $n = 5$.

as a consequence, the average magnetic anisotropy of the particle is very small. In view of that, it will be neglected in our calculations [32, 33].

For different values of n we can determine the ranges of values of the dimensionless radius R/l_x and length W/l_x within which one of the three configurations is of lowest energy. The boundary line between any two configurations can be obtained by equating the expressions for the corresponding total energies. Figure 4 illustrates phase diagrams for $d = l_x$, $\beta = 0.5$, and $n = 1$ (solid lines), 3 (dotted lines), and 5 (dashed lines). It is important to observe that for the Fz and Fx states the exchange energy is the same. Then, in the absence of applied magnetic fields and crystalline anisotropies, the dipolar energy is fundamental in obtaining the magnetic configuration of lowest energy. Thus, the dipolar contribution represents the shape anisotropy and for multisegmented nanostructures with a small length (namely nanorings) the low energy state is the quasi-uniform in-plane configuration Fx [25]. As the length is increased, but keeping the radius small enough, there is a transition to the out-of-plane state Fz at a critical length whose value depends on R , β , and the exchange length l_x . As the radius is increased, the magnetizations turns to the vortex configuration at a critical radius depending on the values of W , β , and l_x . Finally, by comparing our results we observe differences in the behavior of the triple point as a function of n . The triple point occurs for smaller R/l_x when n is decreased.

Similar to the case of a single ring, the phase diagram changes with β [25]. The dependence of the whole diagram on the value of n can be investigated by looking at the trajectories of the triple point in the RW plane as functions of β . Such trajectories are shown in figure 5 for $d = l_x$ and different values of n . We remark that the radius R_t of the triple point represents the smallest value of R for which the vortex configurations are stable, and W_t is the largest value of W for which the in-plane configurations are stable.

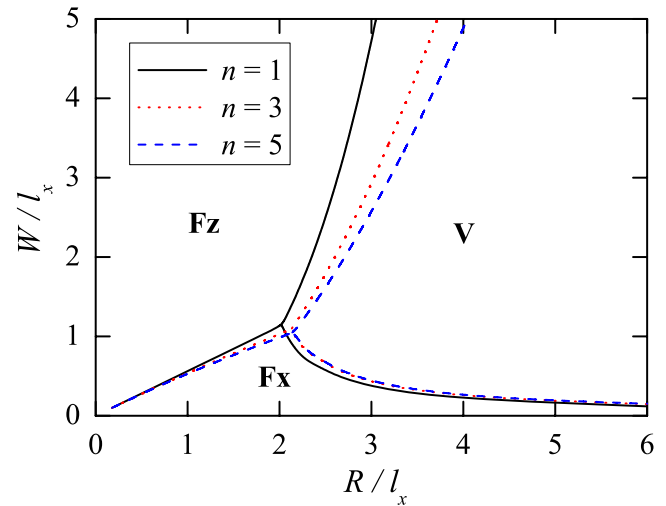


Figure 4. Phase diagrams for barcode-type nanostructures with $\beta = 0.5$ and $d = l_x$.

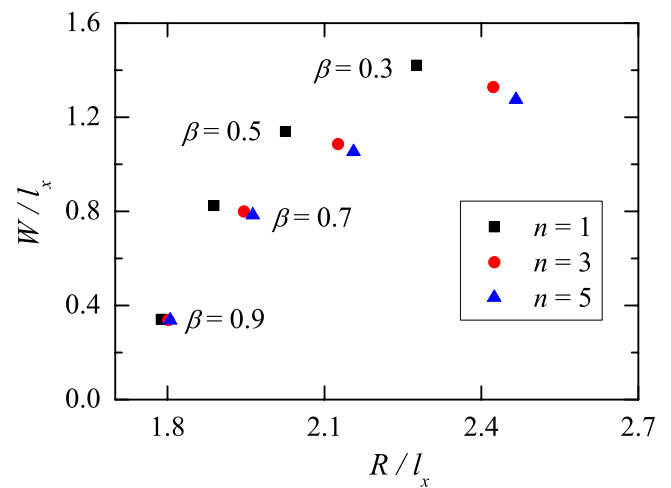


Figure 5. Trajectories of the triple point in the phase diagrams in figure 4 as functions of β , for $n = 1$ (squares), 3 (circles), and 5 (triangles).

2.3. Phase diagram for multisegmented nanotubes

As the multisegmented tubes that motivate this work [14] satisfy $W/R \gg 1$, then the Fx phase can be left out of consideration. Thus, to obtain an expression for the transition line separating the Fz phase from the V phase we match the expressions for the energy of these two configurations. It is important to mention that, for tubes with long radius, a third state, which is a mixture of the other two and has been called *bamboo* or *mixed* state [34–37], has been observed. As is well known, the consideration of non uniform magnetic configurations considerably complicates the calculations and for simplicity, we studied multisegment magnetic nanotubes whose radii are not large enough to allow the formation of relevant vortex domains at the extremes of the tube. Figure 6 presents the transition line for $n = 1$ and 2. To the left of each line the Fz state prevails while to the right of the same line the vortex V configuration is more stable. The

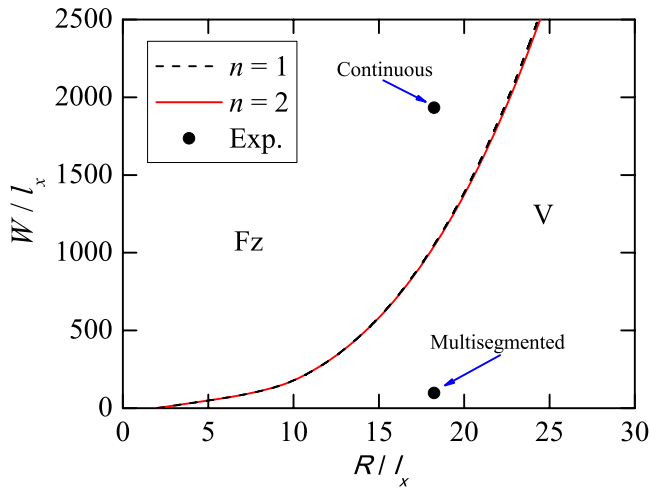


Figure 6. Magnetic phase diagrams of non-interacting multisegmented nanotubes for different values of n . The dimensions of the tube, W and R , are normalized to the exchange length l_x . Experimental points are discussed in the text.

dots labeled (*continuous*) and (*multisegmented*) in figure 6 correspond to the cases of the two hysteresis curves reported in the experimental paper by Lee *et al* [14] defined by (*continuous*) $n = 1$, $R = 150$ nm, $W = 16$ μm , $\beta = 0.75$, and $l_x = 8.225$ nm; (*multisegmented*) $n = 2$, $R = 150$ nm, $W = 800$ nm, $d = 4800$ nm, $\beta = 0.75$, and $l_x = 8.225$ nm. It is important to note that the transition line for $n = 1$ is almost equal to the one for $n = 2$. This is due to the large average distance between the neighboring Ni segments ($d = 4.8$ μm) which avoids interaction effects. From this figure we can conclude that the multisegmented system is well inside the V phase while the continuous system is inside the Fz phase. It allows us to understand why the experimental samples show a different magnetic behavior; they simply have substantial differences in the length of their ferromagnetic segments.

The results presented above may be generalized. We now proceed to investigate the transition line separating the Fz phase from the V phase. To obtain an expression for this transition line we match the expressions for the energy of these two configurations. This leads to $W/l_x = \alpha(\beta, n, d) \times R^3/l_x^3$. Function $\alpha(\beta, n, d)$ is plotted in figure 7. Care must be applied in the limits of the intervals for β . In particular, when β goes to 1 we deal with extremely narrow nanotubes, where eventual surface roughness and thickness irregularities of the nanotubes become important. On the other side, when β goes to zero we are approaching the limit of a solid cylinder, where the core in the vortex phase becomes important and must be considered to get the solution. As the multisegmented nanotubes considered experimentally have $\beta \approx 0.75$, we have neglected these two cases.

3. Conclusions

In conclusion, we have studied the relative stability of ideal configurations of magnetic barcode-type tubular nanostructures composed of alternate ferromagnetic and nonmagnetic layers. In such systems we investigated the size range of the geometric parameters for which different

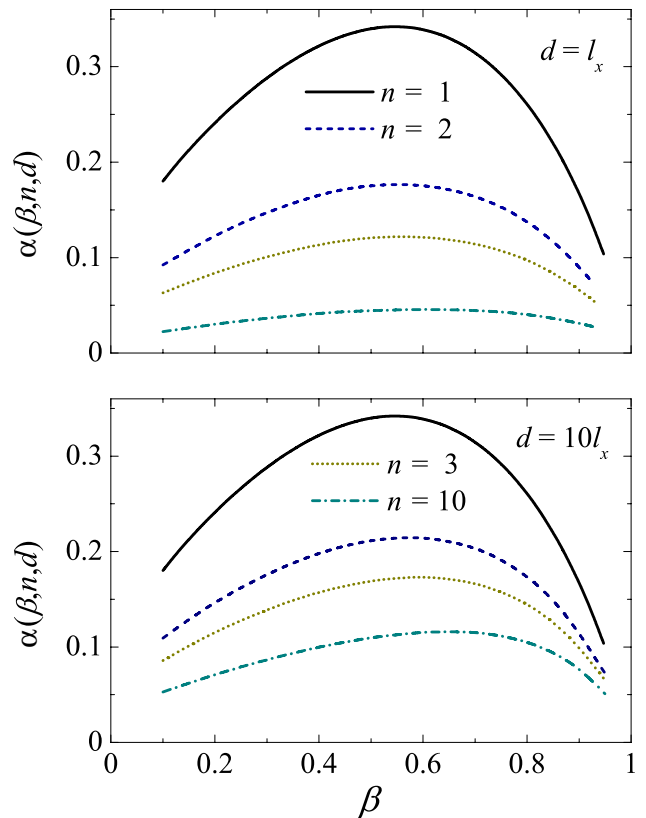


Figure 7. Function $\alpha(\beta, n, d)$ defining the transition condition from the phase diagram of a multisegmented nanotube.

configurations are of lowest energy. Results are summarized in phase diagrams which clearly indicate that the magnetic behavior of such structures can be tailored to meet specific requirements provided a judicious choice of such parameters is made. The lines separating the magnetic phases and, in particular, the triple point, are very sensitive to the geometry of the barcode-type nanostructures. The phase diagrams presented can provide guidelines for the production of nanostructures with technological purpose.

Acknowledgments

We thank D Altbir and K Nielsch for useful discussions. This work was partially supported by FONDECYT grant numbers 11070010 and 11080246, Financiamiento Basal para Centros Científicos y Tecnológicos de Excelencia, Millennium Science Initiative under Project P06-022-F, the program ‘Bicentenario en Ciencia y Tecnología’ PBCT under project PSD-031 and the internal Grant USM-DGIP 11.08.57. We also acknowledge support from the grant program AGCI, CONICYT, and the program PIIC2009 USM (Chile).

References

- [1] Sun S, Murray C B, Weller D, Folks L and Moser A 2000 *Science* **287** 1989
- [2] Koch R H, Deak J G, Abraham D W, Trouilloud P L, Altman R A, Lu Yu, Gallagher W J, Scheuerlein R E, Roche K P and Parkin S S P 1998 *Phys. Rev. Lett.* **81** 4512

- [3] Cowburn R P, Koltsov D K, Adeyeye A O, Welland M E and Tricker D M 1999 *Phys. Rev. Lett.* **83** 1042
- [4] Wolf S A, Awschalom D D, Buhrman R A, Daughton J M, von Molnár S, Roukes M L, Chtchelkanova A Y and Treger M 2001 *Science* **294** 1488
- [5] Gerrits Th, van den Berg H A M, Hohlfeld J, Bar L and Rasing Th 2002 *Nature* **418** 509
- [6] Emerich D F and Thanos C G 2003 *Expert Opin. Biol. Ther.* **3** 655
- [7] Puentes V F, Krishnan K M and Alivisatos A P 2001 *Science* **291** 2115
- [8] Eisenstein M 2005 *Nat. Methods* **2** 484
- [9] Yanagishita T, Sasaki M, Nishio K and Masuda H 2004 *Adv. Mater.* **16** 429
- [10] Wu G, Zhang L, Cheng B, Xie T and Yuan X 2004 *J. Am. Chem. Soc.* **126** 5976
- [11] Mu C, Yu Y, Wang R, Wu K, Xu D and Guo G 2004 *Adv. Mater.* **16** 1550
- [12] Bachmann J, Jing J, Knez M, Barth S, Shen H, Mathur S, Gosele U and Nielsch K 2007 *J. Am. Chem. Soc.* **129** 9554
- [13] Escrig J, Bachmann J, Jing J, Daub M, Altbir D and Nielsch K 2008 *Phys. Rev. B* **77** 214421
- [14] Lee W, Scholz R, Nielsch K and Gosele U 2005 *Angew. Chem. Int. Edn* **44** 6050
- [15] Nicewarner-Peña Sheila R, Griffith Freeman R, Reiss B D, He L, Peña D J, Walton I D, Cromer R, Keating C D and Natan M J 2001 *Science* **294** 137
- [16] Lehmann V 2002 *Nat. Mater.* **1** 12
- [17] Nicewarner-Peña S R, Carado A J, Shale K E and Keating C D 2003 *J. Phys. Chem. B* **107** 7360
- [18] Stoermer R L, Cederquist K B, McFarland S K, Sha M Y, Penn S G and Keating C D 2006 *J. Am. Chem. Soc.* **128** 16892
- [19] Jun Son S, Reichel J, He B, Schuchman M and Bok Lee S 2005 *J. Am. Chem. Soc.* **127** 7316–7317
- [20] Albrecht M, Hu G, Moser A, Hellwig O and Terris B D 2005 *J. Appl. Phys.* **97** 103910
- [21] Escrig J, Landeros P, Altbir D, Bahiana M and d'Albuquerque e Castro J 2006 *Appl. Phys. Lett.* **89** 132501
- [22] Aharoni A 1996 *Introduction to the Theory of Ferromagnetism* (Oxford: Clarendon) chapter 7
- [23] See, for example Bloemen P J, Johnson M T, van de Vorst M T H, Coehoorn R, de Vries J J, Jungblut R, van de Stegge J, Reinders A and de Jonge W J M 1994 *Phys. Rev. Lett.* **72** 764
- [24] Beleggia M, Lau J W, Schofield M A, Zhu Y, Tandon S and De Graef M 2006 *J. Magn. Magn. Mater.* **301** 131–46
- [25] Landeros P, Escrig J, Altbir D, Bahiana M and d'Albuquerque e Castro J 2006 *J. Appl. Phys.* **100** 044311
- [26] Escrig J, Landeros P, Altbir D, Vogel E E and Vargas P 2007 *J. Magn. Magn. Mater.* **308** 233–7
- [27] Escrig J, Landeros P, Altbir D and Vogel E E 2007 *J. Magn. Magn. Mater.* **310** 2448–50
- [28] Rothman J, Klaui M, Lopez-Diaz L, Vaz C A F, Bleloch A, Bland J A C, Cui Z and Speaks R 2001 *Phys. Rev. Lett.* **86** 1098
- [29] Usov N A and Peschany S E 2004 *J. Magn. Magn. Mater.* **130** 275
- [30] Escrig J, Allende S, Altbir D and Bahiana M 2008 *Appl. Phys. Lett.* **93** 023101
- [31] O'Handley R C 2000 *Modern Magnetic Materials* (New York: Wiley)
- [32] Klaui M, Vaz C A F, Lopez-Diaz L and Bland J A C 2003 *J. Phys.: Condens. Matter* **15** R985
- [33] Castaño F J, Ross C A, Eilez A, Jung W and Frandsen C 2000 *Phys. Rev. B* **69** 144421
- [34] Wang Z K *et al* 2005 *Phys. Rev. Lett.* **94** 137208
- [35] Landeros P, Suarez O J, Cuchillo A and Vargas P 2009 *Phys. Rev. B* **79** 024404
- [36] Lee S, Suess D, Schrefl T, Oh K H and Fidler J 2007 *J. Magn. Magn. Mater.* **310** 2445
- [37] Chen A P, Usov N A, Blanco J M and Gonzalez J 2007 *J. Magn. Magn. Mater.* **316** e317